Journal of Crystal Growth 408 (2014) 32–41

Contents lists available at ScienceDirect

Journal of Crystal Growth

journal homepage: www.elsevier.com/locate/jcrysgro

Evaluation of growth methods for the heteroepitaxy of non-polar (11$\bar{2}$0) GAN on sapphire by MOVPE

F. Oehler [a,1], D. Sutherland [b], T. Zhu [a], R. Emery [a], T.J. Badcock [b], M.J. Kappers [a], C.J. Humphreys [a], P. Dawson [b], R.A. Oliver [a,*]

[a] Department of Materials Science and Metallurgy, University of Cambridge, Cambridge CB3 0FS, United Kingdom
[b] School of Physics and Astronomy, Photon Science Institute, University of Manchester, M13 9PL Manchester, United Kingdom

ARTICLE INFO

Article history:
Received 12 June 2014
Received in revised form
30 August 2014
Accepted 5 September 2014
Communicated by M. Weyers
Available online 16 September 2014

Keywords:
A1. Defects
A1. Characterization
A3. Metalorganic vapor phase epitaxy
B1. Nitrides

ABSTRACT

Non-polar *a*-plane gallium nitride (GaN) films have been grown on *r*-plane (1$\bar{1}$02) sapphire by metal organic vapour phase epitaxy (MOVPE). A total of five *in situ* defect reduction techniques for *a*-plane GaN are compared, including two variants with a low temperature GaN nucleation layer (LTNL) and three variants without LTNL, in which the high-temperature growth of GaN is performed directly on the sapphire using various crystallite sizes. The material quality is investigated by photoluminescence (PL), X-ray diffraction, cathodoluminescence, atomic force and optical microscopy. It is found that all layers are anisotropically strained with threading dislocation densities over 10^9 cm^{-2}. The PL spectrum is typically dominated by emission from basal plane stacking faults. Overall, growth techniques without LTNL do not yield any particular improvement and even result in the creation of new defects, i.e. inversion domains, which are seldom observed if a low temperature GaN nucleation layer is used. The best growth method uses a LTNL combined with a single silicon nitride interlayer.

1. Introduction

Hexagonal gallium nitride (GaN) presents two stable growth directions inclined at 90° angle to the *c*-direction. Respectively named *a* for [11$\bar{2}$0] and *m* for [1$\bar{1}$00], these growth directions are referred to 'non-polar' as they are perpendicular to the piezoelectric and spontaneous dipole moments along the *c*-axis [1]. Hence, it is possible to grow quantum wells with an absence of an internal electrical field along these directions [2,3]. For (Al)(In)GaN quantum wells or dots grown on these planes, the quantum confined Stark effect is thus theoretically prevented, leading to shorter radiative lifetimes [4] and a potentially higher efficiency [5]. In-plane anisotropic strain is also present in *a*-plane or *m*-plane non-polar heterostructures, due to the different lattice mismatch respectively along the in-plane *c* and *m*, or *c* and *a* directions. This effectively lifts the spatial degeneracy of the valence subbands [6] and results in the emission of linearly polarised light for *a*-plane [7] and *m*-plane [8] heterostructures.

In this study, we focus on *a*-plane GaN, as this orientation can be grown on *r*-plane sapphire [9,10] using metal organic vapour phase epitaxy (MOVPE). High quality *a*-plane GaN bulk substrates are commercially available [11], but their current high price restricts their use to research projects or high value devices. Therefore numerous efforts [12] have been made to achieve hetero-epitaxial *a*-plane GaN on *r*-plane sapphire of a similar quality to *c*-plane GaN on *c*-sapphire.

Many of the *a*-plane GaN *in situ* defect reduction techniques are inspired by standard *c*-plane recipes [13]: the use of GaN low-temperature nucleation layers (LTNLs) grown in hydrogen or nitrogen carrier gas [14–17], high- or low-temperature aluminium nitride nucleation layers [14,18–20] and the deliberate delay of island coalescence via three dimensional to two dimensional growth mode transitions (3D2D) [21,22,17]. Some other techniques, also derived from *c*-plane recipes, are based on growth interruptions by the inclusion of interlayers: single or multiple silicon nitride (SiN_x) interlayers [23,24,21,17] or scandium nitride interlayers [25], which can be followed by a 3D growth step [12]. Lastly, novel growth techniques have been explored, such as high silicon doping [26] or epigrowth without the use of a nucleation layer, i.e. 'direct growth' on *r*-plane sapphire at high temperature [27–29].

Despite the large variety of approaches, the overall success has been limited. Typical, *a*-plane GaN layers grown on *r*-plane sapphire show numerous basal plane stacking faults (BSFs) with a density of the order of 10^5 cm^{-1}. In addition to BSFs, the typical threading dislocation densities (TDDs) are above 10^9 cm^{-2} [17], whereas *c*-plane GaN layers usually show only TDDs around 10^7–10^8 cm^{-2} and no BSFs [13]. It is possible to reduce these

* Corresponding author.
E-mail addresses: fabrice.oehler@lpn.cnrs.fr (F. Oehler), rao28@cam.ac.uk (R.A. Oliver).
[1] Current address: CNRS – Laboratoire de Physique et de Nanostructures, Route de Nozay, 91460 Marcoussis, France.

http://dx.doi.org/10.1016/j.jcrysgro.2014.09.009

numbers using patterned substrates [12] but at the cost of complex initial processing steps and a larger buffer thickness. In this case, wafer bowing becomes problematic [30], due to the thermal mismatch between GaN and sapphire, which creates large thermal gradients across the surface. This leads to a poor homogeneity, particularly in the subsequent growth of heteroepitaxial layers. This issue provides a strong motivation to understand and improve *in situ* defect reduction techniques for hetero-epitaxial *a*-plane GaN.

In this work, we investigate the impact of low-temperature nucleation layers on the material quality, by comparing direct three-dimensional growth on *r*-plane sapphire [27–29] (without a nucleation layer), with more established procedures which involve the use of a low-temperature GaN nucleation layer (LTNL), combined with either a SiN_x interlayer or a 3D to 2D growth transition. We also consider the impact of the reactor conditions of the 3D layer grown directly on sapphire on the structural quality of the resulting *a*-plane GaN epilayer.

2. Experimental

The *a*-plane $(11\bar{2}0)$ GaN layers are grown using a Thomas Swan 6×2 in metal-organic vapour phase epitaxy (MOVPE) reactor on commercial *r*-plane $(1\bar{1}02)$ sapphire wafers (Kyocera) with $0.25 \pm 0.1^\circ$ miscut off to *a*-plane. The gallium and indium precusors are trimethylgallium (TMG) and trimethylindium (TMI) respectively. The nitrogen source is ammonia (NH_3) and the silicon source is silane (SiH_4) dilluted in hydrogen (H_2). The total reactor flow is kept constant at 20 standard litres per minute (SLM) by balancing the flow rates of the carrier gas and NH_3. Unless otherwise specified, the total reactor pressure is 100 Torr and H_2 is used as the carrier gas. The growth temperatures quoted are that of the sample susceptor, as measured by an emissivity-corrected pyrometer (Laytec) operating at 950 nm, calibrated against a black-body source.

Prior to the actual growth, all processes are initiated by annealing the sapphire substrate in NH_3 (3 SLM) at 1050 °C for 8 min. Then, for samples using a low temperature nucleation layer (LTNL), the temperature is ramped down to 550 °C, the LTNL is grown using TMG (90 μmol/min) and NH_3 (1.5 SLM) at 500 Torr for 140 s. Depending on the recipe, a 2D growth step can then be used to achieve planar growth: TMG (610 μmol/min) and NH_3 (0.8 SLM, V:III ratio of 60) at 1030 °C. Alternatively, a 3D growth step can be used to generate faceted islands: TMG (240 μmol/min) and NH_3 (10 SLM, V:III ratio of 1900) at 1050 °C at 300 Torr.

All samples have a final thickness of ca. 4.5 μm. The five different growth procedures are described below and the samples are named in the text after the acronym of their growth method:

- *LT-SiN*: Following the anneal of the sapphire, a LTNL is used and then a 600 s 2D growth steps is carried out. A single SiN_x interlayer is then grown at 900 °C using SiH_4 (0.2 μmol/min) and NH_3 (10 SLM) for 180 s. Following 360 s of subsequent 3D growth, the sample surface is planarised using 2D growth conditions for 1860 s.
- *LT-3D* : Following the growth of a LTNL, a 3D growth step is carried out for 600 s [22], after which the surface is planarised using 2D growth for 2100 s.

Three other samples are grown using *direct* growth methods in which the GaN epigrowth is performed at high temperature, without a LTNL, directly after the sapphire annealing step:

- *d3D*-300 : Growth is directly initiated with a 3D step at 300 Torr for 600 s, followed by 2D growth for 2100 s.
- *d3D*-100 : An alternative approach to the method above involves the 3D growth step being carried out at reduced pressure (600 s, 100 Torr), followed by 2D growth for 2100 s.
- *d3D-Si* : Here, the 3D islands grown directly on the sapphire are highly doped with Si above 10^{19} cm^{-3} [26]. Growth starts with a short undoped 3D step (60 s) to initiate GaN island formation and then continues for 600 s with an additional silane flux under the following conditions: TMG (170 μmol/min) NH_3 (0.8 SLM, V:III ratio of 210) and SiH_4 (0.2 μmol/min), a temperature of 1050 °C and a pressure of 100 Torr. The total flow is reduced to ~6 SLM with H_2 (5 SLM) for this specific step, in which the growth of highly Si-doped 3D islands occurs. The complete procedure is thus sapphire annealing, 3D growth (60 s), highly Si-doped 3D growth (660 s), 2D growth (2100 s).

Finally, all the samples are terminated with a surface treatment using SiH_4 (0.2 μmol/min) and NH_3 (8.2 SLM) at 860 °C for 240 s to increase the size of the pits related to threading dislocations at the sample surface. This technique has been primarily developed for the analysis of (0001) GaN layers by atomic force microscopy [31] but has also been applied previously for *a*-plane GaN [32].

An $In_xGa_{1-x}N$ layer was grown on one sample without a SiH_4 surface treatment. Growth of a single InGaN layer is the very first step toward GaN-based light emitting diodes (LEDs). The different chemical nature of the InGaN layer also affects the surface termination of extended defects. For example, the dislocation pits found at the surface of a *c*-plane InGaN layer are often much larger that those appearing on GaN layer [33]. Here, the *a*-plane $In_xGa_{1-x}N$ growth was performed for 2500 s at 710 °C and 300 Torr using TMI (8 μmol/min), TMG (6 μmol/min) and NH_3 (10 SLM) with nitrogen N_2 (10 SLM) as a carrier gas. The InGaN thickness is approximately 40 nm. X-ray diffraction reciprocal space maps of the 110, 201 and 300 reflections show that the $In_xGa_{1-x}N$ layer is fully strained and that the composition is $x = 0.045 \pm 0.005$.

The surfaces of the samples were observed using differential interference contrast (DIC) optical microscopy (also known as Normarski microscopy). Atomic force microscopy (AFM) was performed using a Veeco Dimension 3100 in tapping mode using 'rotated tapping mode etched silicon probes' (RTESP) with a nominal end radius of 8 nm.

Plan-view SEM-CL experiments were performed at room and low temperature (90 K) using a Philips XL30 scanning electron microscope (SEM) operating at 5 kV. This microscope is equipped with a Gatan MonoCL4 system with both photon multiplier tube (PMT) and charge-coupled device (CCD) detectors. The CL spectra are extracted from hyperspectral maps by summing the contribution of each pixel from a homogeneous square area of 1 μm^2 (8×8 pixels). This way, each spectra represents the emission from a chosen zone and the risk of sampling a non-representative defect is minimized.

High resolution X-ray diffraction (XRD) was performed using a Panalytical MRD diffractometer, equipped with a symmetric 4-bounce monochromator and a 3-bounce analyser to select the CuKα1 wavelength. First, a simple symmetric scan with an open detector (no analyser) was acquired over the whole range of ω to check that the sample only consists of *a*-plane GaN, with no other detectable orientation or inclusion. Second, a specific experiment was designed to acquire the rocking curves of the symmetric reflections (110) and (220) in all the in-plane directions, as the anisotropy between the in-plane *c* and *m* directions can be used to qualify the layer quality [24]. To evaluate these properties in a systematic fashion, ω–ϕ maps were acquired for each sample, where ω is the angle between the incident X-ray beam and the sample normal and ϕ the rotation angle around the sample normal. Using this technique, a rocking curve in ω is determined

for each in-plane orientation, for every 2° in ϕ. The in-plane m orientation, $\phi = 0$ on the ω–ϕ map, is determined using the asymmetric (300) reflection. The count rate was normalized with respect to the open-beam count rate for each sample to compensate for the ageing of the Cu cathode (approx. 10% signal decrease between the first and last sample analysis by XRD).

Temperature dependent photoluminescence (PL) spectroscopy was performed using a closed-cycle helium cryostat at 6 K. A continuous wave laser HeCd at 325 nm was used to excite the samples at an energy above the GaN barrier bandgap. The luminescence was focused onto 0.5 mm slits of a 0.85 m double grating spectrometer equipped with a Peltier-cooled GaAs photomultiplier tube. The spectra were recorded with signal lock-in processing techniques.

As the HeCd laser absorption length is ca. 350 nm for 99% absorption in GaN (ignoring any carrier diffusion at 6 K), the photoluminescence experiments only probe the uppermost 350 nm of the sample. Here, the thickness of top-most GaN layer is in excess of 1.5 μm and the same final growth condition ('2D growth') are used for all the samples. The 3D islands, the islands coalescence and the associated defect reduction thus occur far away from the area probed by PL. The PL can then be used to monitor the efficiency of the different defect reduction techniques by sampling the extended defects that remains in the top-most layer.

3. Results

3.1. Surface morphology

All samples were observed using DIC microscopy at different stages of the growth process. The corresponding images are shown Fig. 1. The micrographs in the top row of the figure show the 3D islands prior to the 2D coalescence step for the samples incorporating a 3D to 2D growth transition. This data is not presented for the sample '*LT-SiN*' since it does not use the same kind of 3D–2D transition (the 3D growth time is only 360 s). Depending on the growth method, the 3D layer can show dense and small crystallites or large and scattered crystallites. This is controlled by various means, such as the annealing time of the nucleation layer, if there is one. For direct growth methods, '*d3D-xxx*', the island density can be varied through the pressure at which the 3D growth step is performed, with lower pressures favouring low densities, Fig. 1(c, top) and (d, top). The shape of the crystallites, i.e. the exposed facets and the aspect ratio, can also be altered by the presence of impurities such as high silicon doping, which leads to elongated crystallites aligned along the *c*-direction, Fig. 1(e, top), confirming an earlier report [26].

The micrographs at the bottom row of Fig. 1 show the sample surface after the coalescence stage. The sample surfaces exhibit large-scale undulating features, which are elongated along the in-plane *c*-direction. The feature size relates to the crystallites size at the end of the 3D growth. This morphology is quite common for non-polar GaN layer, for example such 'striations' were described by Sun et al. [34].

The coalesced layers were also investigated by AFM. All samples were found to share similar microscopic morphologies as that shown in Fig. 2(a) (of the '*d3D-Si*' sample), with high densities of shallow dislocation pits and step-like features perpendicular to the *c*-direction, sometimes terminating at dislocation pits. Such characteristics have already been reported [32] and a large fraction of the dislocation pits is believed to originate from partial dislocations (PD). Due to the small variations in height *z*, we present alongside the actual topographic data the simultaneously recorded amplitude error image in Fig. 2(b) (which tends to highlight the region of steep slopes). The average TDD of each sample and its standard deviation, as listed in Table 1, were determined after analysing 4 AFM images ($2 \times 2\ \mu m^2$) per sample, with each image containing over a hundred dislocation pits. The AFM analysis reveals that although all the growth procedures give TDDs in the range of 10^9–$10^{10}\ cm^{-2}$ the three '*d3D*' samples have the lowest TDD while the '*LT-3D*' growth method gives the highest TDD.

3.2. X-ray diffraction

A typical ω–ϕ map of the (110) reflection for the '*d3D-100*' sample is shown Fig. 3(a). It illustrates three key pieces of information: (1) the variation of the full width at half maximum of the rocking curve (ω-FWHM) with the in-plane orientation ϕ (white arrows indicate those of the *m*- and *c*- directions), (2) the variation of the diffracted intensity represented by the colours of the logarithmic colour scale and (3) the shift of the peak position in ω relative to the ideal symmetric configuration $\omega = \theta$ (vertical black line) measured by a positive or negative offset angle (black arrow). The offset angle is related to the (110) plane misalignment with the sample normal [35] and possibly the sapphire wafer

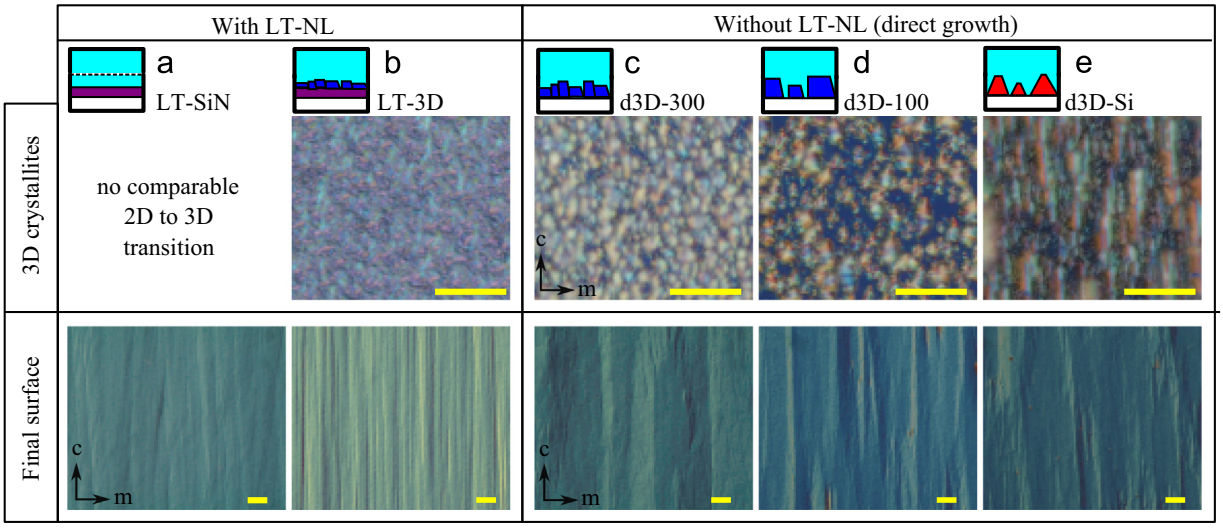

Fig. 1. DIC images of the sample surface before and after the final coalescence (2D growth step). Scale bar (10 μm) and orientation versus the crystalline axes are the same for all images. Depending on the growth method, different crystallites (size, shape, density) are used, top row, prior to the formation of the final surface, bottom row.

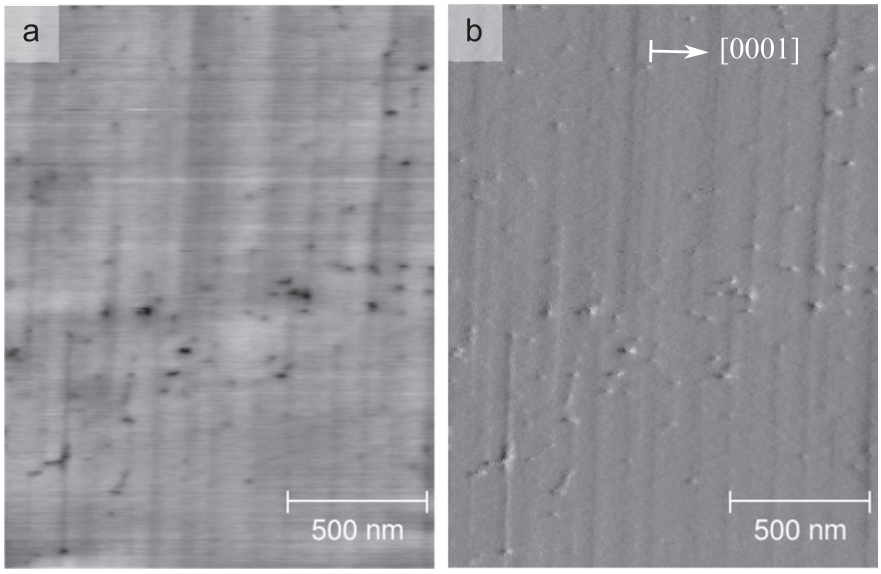

Fig. 2. AFM images of the coalesced surface of the '*d3D-Si*' sample. (a) Topographic image, *z*-scale 5 nm. (b) Corresponding amplitude error image.

Table 1
Threading dislocation densities (TDDs) and standard deviations, statistically determined from four $2\times2\ \mu m^2$ AFM images per sample.

Sample	TDD ($\times 10^9\ cm^{-2}$)
LT-SiN	4.0 ± 0.5
LT-3D	7.0 ± 0.6
d3D-300	2.3 ± 0.6
d3D-100	4.1 ± 0.5
d3D-Si	3.2 ± 0.1

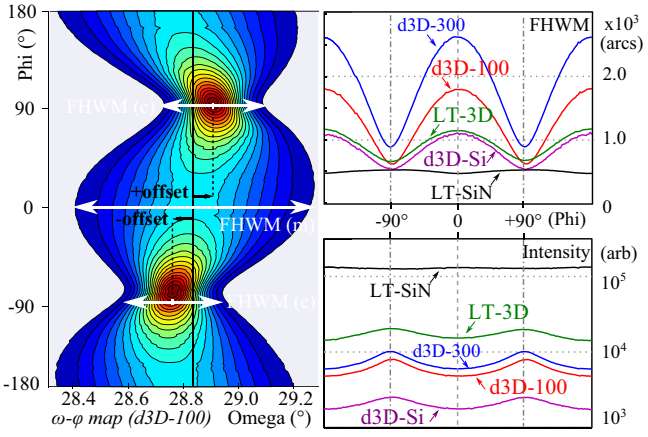

Fig. 3. (a) Omega-phi map of the symmetric reflection (110) of the '*d3D-100*' sample. (b) and (c) Parameters of each sample, ω-FWHM (linear scale) and peak intensity (log scale), issued from the Gaussian fit of the rocking curves.

miscut. Therefore when the offset angle is nil, near $\phi=0$ in this case, the sample is actually misaligned in χ, the angle between the X-ray plane of incidence and the sample surface [35]. To minimise the effect of this misalignment, the XRD diffractometer is operated in a line-focus mode, where the typical FWHM along χ is more than 1.5°. The typical offsets angle in this study are less than 0.25°, which typically results in an error of 5% for the ω-FHWM measurement and the peak intensity at the maximum misalignment. Peak fitting using a pseudo-Voigt function was performed on selected rocking curves and the peaks were all found to be near Gaussian ($>80\%$ Gaussian, $<20\%$ Lorentzian), which is often the case for defective layers. Therefore, a simple Gaussian fit was used to extract the values of the ω-FWHM, Fig. 3(b), and the peak intensity, Fig. 3(c), for all the samples.

Table 2
ω-FWHM of the symmetric reflections (110) and (220), along the *c* and the *m* directions, computed from ω–ϕ maps using a Gaussian fit (see Fig. 3).

Sample	110 (arcs)		220 (arcs)	
	c	*m*	*c*	*m*
LT-SiN	515	460	505	445
LT-3D	660	1150	630	1120
d3D-300	880	2630	870	2650
d3D-100	620	1800	590	1770
d3D-Si	535	1090	530	1080

Fig. 3(b) reveals that samples based on 3D growth, ('*LT-3D*', '*d3D-100*', '*d3D-300*', '*d3D-Si*') with or without a LTNL, all have a highly anisotropic ω-FWHM values. For these samples, the ω-FWHM along the *m*-direction is more than twice of that along the *c*-direction, for which the narrowest ω-FWHM values ($\sim$500 arcs) are found for samples '*LT-3D*' and '*d3D-Si*'. The sample with a silicon nitride interlayer, '*LT-SiN*', behaves quite differently with narrow and near isotropic ω-FWHM values. For this sample, the ω-FWHM variation is small ($\sim$10%) and reversed compared to the other samples: the ω-FWHM along *m* (446 arcs) is lower than along *c* (505 arcs). This effect has been previously observed for similar SiN_x samples [24]. The values of the ω-FWHM for the (110) and the (220) reflections of all the samples are reported in Table 2.

The XRD peak intensity, as shown in Fig. 3(c), follows the inverse variation of the ω-FWHM: a narrow ω-FWHM correlates with a large signal and a large ω-FWHM with a weak signal. The sample '*LT-SiN*', with the narrowest and the most isotropic ω-FWHM, shows a signal more than a decade higher than the other samples.

It can be seen from Table 2 that the ω-FWHM values from the (220) reflection are slightly lower than those of (110) for all positions. Although the differences are small, about 1–3%, they are consistent for all samples. This surprising result is likely due to an artefact in the measurement protocol. To maximise the signal, the X-ray beam width was kept constant (1.2 mm) during the measurements, leading to a larger illuminated area for the (110) reflection (2.5 mm wide, $\omega\simeq28.9°$), than for the (220) reflection (1.3 mm wide, $\omega\simeq74.8°$).

Table 3
Strain measurement by XRD: out-of-plane lattice parameter a, vertical strain, and the anisotropic wafer bow (radii of curvature) along the in-plane m- and c-directions. The negative values of the radii indicate a convex shape.

Sample	a (Å)	$\epsilon_a(\times 10^{-3})$	R_c (m)	R_m (m)
LT-SiN	3.1929	1.13	−2.8	−3.6
LT-3D	3.1917	0.75	−3.7	−7.4
d3D-300	3.1927	1.06	−3.0	−5.4
d3D-100	3.1926	1.03	−3.4	−5.8
d3D-Si	3.1933	1.27	−2.3	−4.7

Together with the small radii of curvature (see Table 3), the large illuminated area for the reflections leads to an overestimation of the ω-FWHM values. As the reflections are very broad, this effect is relatively small: 1–2% widening for the ω-FWHM of the (110) reflections and approximately 0.2–0.5% for the (220) reflections. Other artefacts could also have been introduced during the Gaussian fitting process, due to the large absolute intensity difference between the (220) and (110) reflections. For future analysis, the ω-FWHM of the (110) and (220) reflections are considered equal, within 5% error.

We will now discuss the epilayer strain measurements. The out-of-plane lattice spacing, a, was measured on each sample, using an omega-2theta map of the (220) reflection at room temperature. For the relaxed GaN parameter, we use $a_0 = 3.1893\,\text{Å}$ [36,37], enabling us to compute the vertical component of the strain $\epsilon_a = (a - a_0)/a_0$. For each sample, the anisotropic wafer bow (in the m- and c- directions) was computed from a series of five rocking curves of the (220) reflection following the method described in [38]. The sample was moved by steps of 5 mm. The results are summarized in Table 3.

All samples share similar strain states and anisotropic bowing. The out-of-plane direction is under tensile stress at room temperature which indicates that the wafer is under in-plane compressive stress, at least along one of the in-plane directions. Depending on the sample structure, as well as small thickness variations, the actual strain varies between the layers: the sample '*LT-3D*' shows the smallest strain, the sample '*d3D-Si*' the largest strain, while the other samples ('*LT-SiN*', '*d3D-300*' and '*d3D-100*') have comparable strain. The curvatures of the wafer are all convex [39] and anisotropic [30], with the radius of curvature along the c-direction being roughly half of that along the m-direction. Convex bowing is typically observed for GaN layers grown on sapphire and stems from the thermal mismatch between the GaN layer and the sapphire substrate, as the thermal expansion coefficients of sapphire are larger than those of GaN [30,39,40].

3.3. Photoluminescence

To investigate their optical quality, the samples were studied by photoluminescence at 6 K. In non-polar GaN epilayers, specific defects have been shown to be optically active, such as basal plane stacking faults (BSFs) [41,42].

The normalized spectra for all the samples are shown in Fig. 4. In general two or three emission bands are found in each sample, the GaN near-band edge peak (NBE) near 3.49 eV which we associate to donor bound excitons D^0X [42,30,43], the I_1 BSF peak at 3.44 eV [42], and some weak overlapping emission peaks between 3.25–3.40 eV, which are potentially due to donor-acceptor pair recombination [44] or prismatic staking faults (PSF) [45]. For all samples, the strongest emission peak does *not* originate from the GaN D^0X but from the BSFs. The ratio of the relative intensity of these two peaks (D^0X:BSF) correlates with the BSF density. The spectra in Fig. 4 are normalised to the peak of BSF-related emission and therefore the least defective sample, i.e.

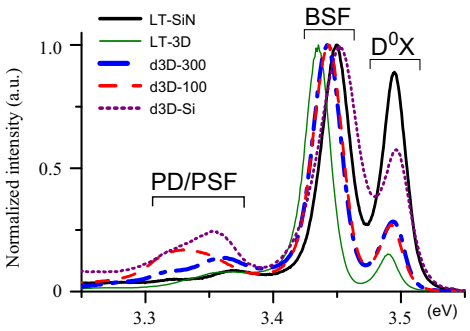

Fig. 4. Low temperature photoluminescence (6 K) spectra of the a-plane GaN samples. Three emission bands are identified, GaN D^0X at 3.49 eV, I_1 BSF at 3.44 eV, other defects (potentially PD or PSF) between 3.25 and 3.40 eV.

Table 4
Comparative PL signal strength (peak values) between the different emission bands: GaN D^0X at ~3.49 eV, I_1 BSF at ~3.44 eV, other defects (PD or PSF) between 3.25 and 3.40 eV.

Sample	D^0X:BSF	D^0X:PD/PSF
LT-SiN	1:1.1	1:0.1
LT-3D	1:6.6	1:0.4
d3D-300	1:3.5	1:0.5
d3D-100	1:3.6	1:0.8
d3D-Si	1:1.7	1:0.5

the one with the smallest BSF density, shows the strongest D^0X peak. At best the ratio of the peak value of the D^0X peak to of the BSF peak is 1–1.12 for the '*LT-SiN*' sample, while it is much lower for the other samples. The values of the ratios D^0X:BSF and D^0X:PD/PSF are summarized in Table 4.

The D^0X peak shift between the different sample correlates well with the XRD strain state measured at room temperature. Fig. 5 shows the energy of the D^0X peak, E_{D^0X}, against the out-of-plane strain ϵ_a from Table 3. The BSF peak energy (not shown) is also observed to shift with the strain.

As reported by Roder et al. [30] on a-plane GaN layers, the D^0X peak energy is known to shift with the stress in the layer. The correlation observed in Fig. 5 between the XRD strain state at room-temperature and the shift of the of the D^0X PL peak at low-temperature can be qualitatively understood as follow. At the growth temperature (~1300 K) the GaN layers are mostly unstrained. At room temperature (XRD ~300 K) the layers are stressed due to the thermal mismatch between the GaN and the sapphire. Further cooling to liquid helium temperature (PL ~6 K) intensifies the existing strain states proportionally to the temperature difference. Consequently, as long as the strain remains in the elastic regime and the temperature difference between the PL and the XRD is constant, the PL energy shift observed at low temperature correlates with the strain state at room-temperature.

3.4. Cathodo-luminescence

The samples were furthermore characterised by SEM-CL at room temperature. Panchromatic CL and SEM images of the sample surface are shown in Fig. 6(a) for the '*LT-SiN*' sample, in Fig. 6(b) for the sample '*d3D-100*' and in Fig. 6(c) for the sample '*d3D-Si*'. The CL images are characterised by bright regions which are bounded by a narrow trench (visible in the SEM). The false coloured '*SUM*' images, generated by summing the SEM (green channel) and the CL (red channel) images, illustrate the fact that all the bright regions are enclosed by narrow ditches. The density and the size of the bright regions depend on the growth methods.

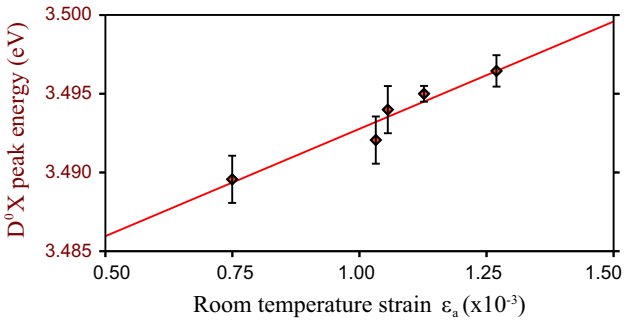

Fig. 5. Variations of the energy of the D^0X peak E_{D^0X} (observed by PL, Table 5) with the out-of-plane strain ϵ_a (measured by XRD, Table 3). The line is the associated linear fit.

Table 5
Peak energies of the BSF and D^0X emissions for the different samples. The typical incertitude due to the peak width is ± 0.0010 eV for the BSF and ± 0.0015 eV for the D^0X.

Sample	E_{D^0X} (eV)	E_{BSF} (eV)
LT-SiN	3.4950	3.4493
LT-3D	3.4896	3.4350
d3D-300	3.4940	3.4421
d3D-100	3.4921	3.4431
d3D-Si	3.4965	3.4522

Small bright regions are observed rather infrequently on the '*LT-SiN*' sample while numerous bright regions are observed on the '*d3D-100*' sample, with the largest ones being observed on '*d3D-Si*' sample. The trenches surrounding those features can be directly observed by optical DIC microscopy, Fig. 6(d) and (f), although some may lie at the resolution limit (Fig. 6(d) arrow).

Spectrum imaging is shown Fig. 7, in which the GaN data is provided by the sample '*d3D-Si*'. For each observation, a single hyperspectral map is acquired, featuring at least a dark area and a bright area. The spectral absolute intensities between those two regions can thus be directly compared. At room temperature, Fig. 7(a), the CL emission of the *a*-plane GaN mainly originates from yellow band YB (ca. 550 nm) for the bright and the dark regions. The signal from the GaN NBE (ca. 360 nm) is barely above the noise level. Similar spectra are observed for the GaN at low temperature (90 K), Fig. 7(b). Despite the lower temperature, the GaN NBE signal is too low to dissociate possible different contributions from the BSF or the D^0X. The absolute intensity ratio of the YB between the bright and dark region is 10:1 at room temperature and 4:1 at low temperature. The very low intensity of the GaN NBE is due to the excessively low V:III ratio ($\sim$60) used during the final 2D growth step [46].

3.5. InGaN growth

Further investigation of the bright regions observed in Fig. 6 was performed by growing a 40 nm thick $In_{0.05}Ga_{0.95}N$ layer on a GaN '*LT-SiN*' sample. During the growth of the InGaN, surface defects such as dislocation pits tend to enlarge [33]. The resulting InGaN layer is shown Fig. 8 using panchromatic CL (90 K) and AFM. An exceptionally large bright region was chosen, so that the same area could be isolated and characterised by CL and AFM. The panchromatic CL image, Fig. 8(a), is similar to that of the GaN layer (Fig. 6(a)–(c)) with a bright region against a dark background.

Spectral imaging at 90 K, Fig. 7(c), reveals that the CL signal has two components: an InGaN related broad band at 400 nm and a yellow band (YB) at 550 nm. Similarly to the GaN spectra, Fig. 7 (a) and (b), the intensity of the YB emission is very strong in the bright region with an intensity ratio of 12:1 between the bright and dark regions. However the InGaN-related emission (ca. 400 nm), Fig. 7(c), is here much stronger the GaN NBE, Fig. 7(b). The intensity ratio of the InGaN emission is 4:1 between the bright and dark regions. The differences in CL signal between the GaN material and the InGaN layer may be due to the growth conditions: standard growth for the InGaN layer compared to very low V:III ratio for the underlying GaN material.

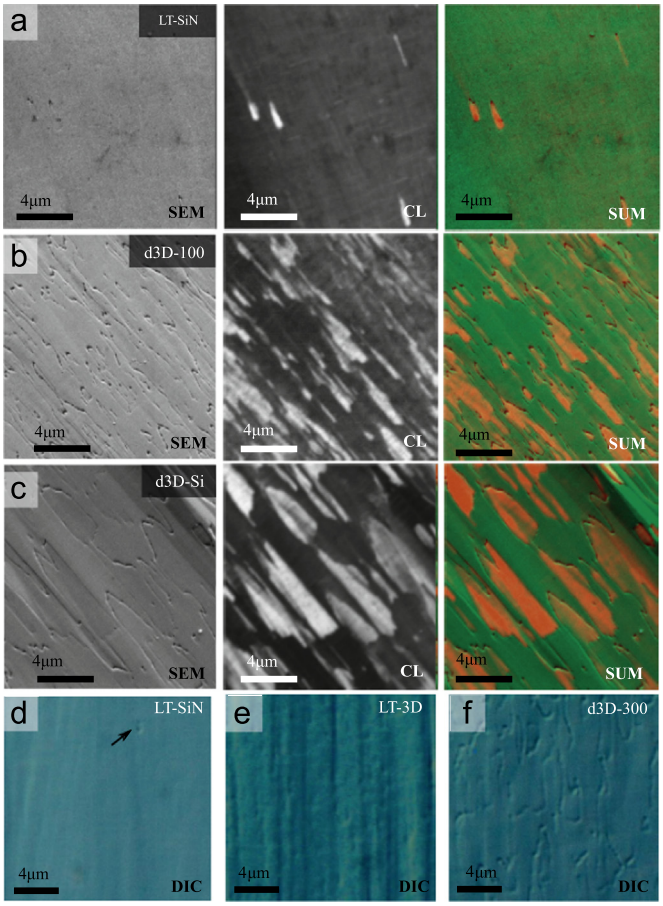

Fig. 6. SEM and room temperature panchromatic CL images for sample '*LT-SiN*' (a), '*d3D-100*' (b) and '*d3D-Si*' (c). The '*SUM*' image to the right is a false color dataset generated by summing color channels from the SEM (green channel) and the CL images (red channel). Images (d)–(f) are high magnification DIC images of the surface of samples '*LT-SiN*' (d), '*LT-3D*' (e) and '*d3D-300*' (f).

The trench bounding the bright regions on the InGaN layer is clearly visible by AFM, Fig. 8(b), and was measured to be at most 50 nm deep. The AFM image, Fig. 8(c), taken at a higher resolution, reveals small hillocks at the surface of the InGaN layer and also shows pits related to the termination of dislocations. Compared to the GaN surface, Fig. 2, the pits in the InGaN layer are larger, deeper, and present a triangular shape (Fig. 8(c), black circles). The orientation of the triangular vertex, pointing up or down, depends on the position of the pits, inside or outside of the bright regions (Fig. 8(c), white arrows).

4. Discussion

Here, we examine the results of the various characterisation techniques applied to the *a*-plane GaN epilayer samples grown using the five different MOVPE methods and we attempt to find parallels in their respective outcomes. In the process, we hope to

determine which growth method produces the highest quality GaN epilayer.

We observe no obvious correlation when comparing the samples' anisotropy in the XRD ω-FWHM of the symmetric reflection along *c* and *m* with their respective threading dislocations densities (TDDs) determined from AFM (see Tables 1 and 2). For instance, the three direct growth samples '*d3D-xxx*' have the lowest TDDs as well as the highest anisotropy in XRD linewidth. Correlation between the values of the XRD linewidth and the TDD is also not supported by the data from both groups of sample, with and without LTNL. Also, the two samples with similar ω-FWHM values, '*LT-3D*' and '*d3D-Si*', differ in TDD by a factor of 2.

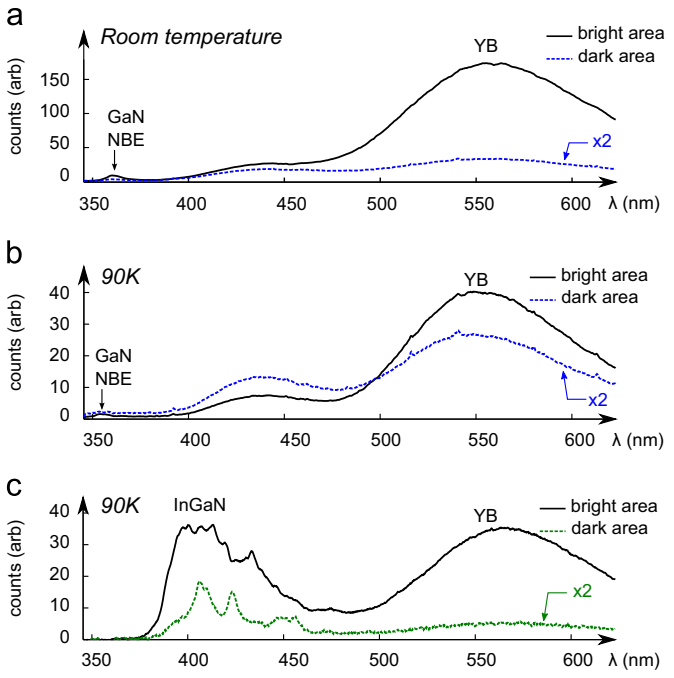

Fig. 7. CL spectra of bright and dark regions. (a) GaN at room temperature. (b) GaN at 90 K. (c) InGaN at 90 K. The signals from the dark areas are all multiplied by a factor 2. (For interpretation of the references to color in this figure caption, the reader is referred to the web version of this article.)

Furthermore, there seems to be no correlation between the XRD linewidths and the D^0X:BSF ratio from PL (see Tables 2 and 4). The latter is not surprising as the XRD symmetric reflections (110) and (220) are not sensitive to the phase translation induced by stacking faults [47,48]. This absence of correlation between XRD ω-FWHM and the BSF density is further reinforced by the equal values of the ω-FWHM of the (110) and (220), for all in-plane directions (Table 2), indicating that no limited lateral coherence length is broadening the peak in our samples. Anisotropic wafer bowing is not a likely reason either, as the curvature (Table 3) is higher along *c* while the XRD ω-FWHM is generally lower in this direction.

The GaN surface roughness, which is noticeable in the optical micrographs in Fig. 1, can also impact the XRD line-width. Surface roughness distorts the thickness fringes perpendicularly to the surface normal, which lies along ω–2θ scan direction for symmetric reflections, (110) and (220). This effect should not be visible in our data, Fig. 3, as the ω-scan axis is nearly orthogonal to the ω–2θ for symmetric reflections [35]. Excessive surface roughness can lead to partial relaxation of the film [48]. Here, symmetric reflections are naturally insensitive to in-plane (lateral) micro-strain due to geometrical considerations, but the out-of-plane micro-strain can still broaden the reflections along the sample normal. For symmetric reflections, this broadening also occurs along the ω–2θ axis, perpendicularly to the ω-scan direction, and therefore should not affect our data. Consequently, the sample roughness observed after growth does not impact directly the specific XRD parameters studied here (FWHM anisotropy of the ω-scan of symmetric reflections) but it could still correlate with other core material properties (specific defects or dislocations) which could affect the ω-FWHM. After eliminating the effects of some known parameters (wafer curvature, lateral coherence length, threading dislocation densities, staking faults densities) and in the absence of a more precise physical description, we can only attribute the different broadening of the (110) and the (220) reflection to a different microstructure and a generic 'anisotropic mosaic tilt'. Moram et al. [48] have also highlighted the absence of simple correlation between the defect densities of *a*-plane GaN and the XRD linewidth of selected symmetric and asymmetric reflections.

The TDDs measured by AFM (Table 1) do not correlated well with D^0X:BSF ratios (Table 4), despite the previous observation that a significant fraction of the TDs are partial dislocations (PDs)

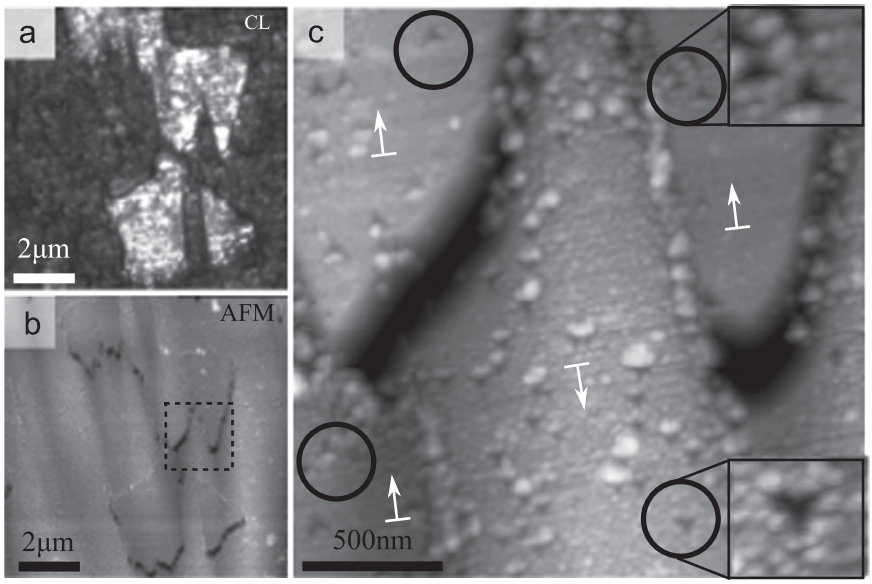

Fig. 8. Surface of 40 nm InGaN layer grown on '*LT-SiN*' GaN. (a) Panchromatic CL image (90 K 5 kV) of a bright region. (b) Corresponding AFM image, *z*-scale 100 nm. (c) AFM image, *z*-scale 50 nm, of the region enclosed by the dotted rectangle of image (b). The black circles indicate specific triangular pits and the white arrows the orientation of the triangular vertex. The two zoomed-in areas highlight the two observed orientations.

for TDDs below $6 \times 10^9\,cm^{-2}$ [32]. Whilst PDs appear at the termination of BSFs, any attempt to correlate the BSF density would require more detail, such as the typical length of the BSF segments. This last parameter is likely to differ from sample to sample, considering the various crystallite sizes and densities observed during the initial stages of growth (see Fig. 1).

Although the growth methods employed here are quite varied (sample are grown with or without a LTNL, with different morphologies of the crystallites at the 3D growth step including varying sizes, shape and areal densities), the material quality remains low in comparison to *c*-plane GaN. In particular the '*d3D-Si*' sample, did not outperform the other samples in the BSF density measurement by PL (D^0X:BSF ratio) despite some evidence in the literature of BSF reduction in heavily Si-doped *a*-GaN observed by CL [26]. The photoluminescence data presented here suggest that the sample with the lowest BSF density is the '*LT-SiN*' sample, which a previous study [17] suggests has a BSF density of about mid $10^5\,cm^{-1}$.

Nevertheless, some general trends can be observed between the two groups of samples: the 'bright regions' observed in Fig. 6 correlate well with the presence ('*LT-SiN*', '*LT-3D*') or absence ('*d3D-100*','*d3D-300*','*d3D-Si*') of a low temperature GaN nucleation layer (LTNL). Further investigations based on the InGaN sample, Fig. 8, reveal that the surface pits are rotated by 180° between the bright regions and the darker matrix. Asymmetric 'triangular' or 'kite-shaped' pits related to threading dislocations are typical of non-polar (In)GaN surfaces. The actual shape relates to the anisotropy of the surface energy between the $+c$ and the $-c$ direction [49] and for *a*-plane GaN layers, the triangular vertex points in the $+c$ direction. The rotation of the pits by 180° between the matrix and the bright regions of the InGaN layer demonstrates that the latter are inversion domains (IDs). The trench around the domains, Fig. 8 (a), is then the surface termination of the inversion domain boundary. As the InGaN layer is grown epitaxially on the GaN surface, a reasonable hypothesis is that some (perhaps most) of the IDs found at the top of the InGaN layer originates from the underlying GaN layer. From this hypothesis and the comparable CL properties observed in Figs. 6–8, we conclude that the bright regions observed by CL on the top of the GaN layer are IDs.

XRD symmetric scans over the whole range of ω (not shown) from the sample with the largest density of bright regions ('*d3D-Si*') only show *a*-plane GaN and *r*-plane sapphire reflections. This suggests that the bright regions are also *a*-plane GaN material, which supports the previous conclusion.

The stark contrast observed by CL between the IDs and the layer (Fig. 6) mostly originates from yellow band emission, which is known to be impurity related [50]. This suggests a higher impurity incorporation rate inside the IDs during the low V:III ratio growth. However, unlike *c*-plane IDs which exhibit a different surface chemistry and impurity incorporation rate [51], *a*-plane IDs only differ from the surrounding matrix by the reversal of the in-plane orientation. Consequently, the top surface of the *a*-plane IDs should be of the same chemical nature as the rest of the *a*-plane layer. It is thus unclear why any impurity incorporation or related CL should be different. Indeed, the InGaN emission wavelength is similar inside and outside of the IDs, Fig. 7(c), which indicates a comparable In incorporation inside and outside of the IDs. Different light extraction could explain the changes in the CL intensity but it is rather unlikely that this would affect differently the InGaN emission and the YB. Yet the intensity ratio between the bright and dark regions is very different, 4:1 for the InGaN compared to 12:1 for the YB. The peculiar CL emission observed from the *a*-plane GaN IDs grown at very low V:III ratio remains thus unexplained.

In a simple attempt to quantify the presence of IDs, we compute the 'fraction of inverted surface', f_{id}. The latter is calculated from the CL images by computing the percentage of the surface occupied by the bright regions over the total area. The corresponding values are summarised in Table 6, after the analysis of two CL images (25×25 μm) for each sample of the '*d3D-xxx*' group. For the sample '*LT-SiN*' and '*LT-3D*', DIC microscopy (Fig. 6(d) and (e)) are used instead of CL images, due to the extremely low density of IDs. No value could be measured for sample '*LT-3D*', as the surface morphology does not allow for an easy ID identification from the DIC images, Fig. 6(e), and neither could IDs be found by CL or AFM.

Table 6
Fraction of inversion domains at the sample surface, f_{id}, from the CL and DIC images (cf. Fig. 6).

Sample	f_{id}
LT-SiN	< 1%
LT-3D	/
d3D-300	30–35%
d3D-100	23–27%
d3D-Si	37–41%

Qualitatively, the surface area of a typical ID in each sample scales with the size of the 3D crystallite before coalescence as shown in Fig. 1. Large IDs are found for large 3D crystallites, '*d3D-Si*' (Figs. 1 and 6(c)), while smaller IDs are found for smaller crystallites, '*d3D-100*' (Figs. 1 and 6(b)). For the GaN films that are grown directly on sapphire, this suggests that the inversion domains are generated during the first stages of the 3D growth step and that they simply enlarge during the coalescence process (2D growth step). It is clear that the films grown with a LTNL show a near-absence of IDs. A reversal of polarity in (0001) GaN films is generally associated with the extent of nitridation of the sapphire surface and the annealing of the LTNL [52,53]. Adapting this knowledge to the case of *r*-plane sapphire, it can be inferred that the inversion domains are formed in those *a*-plane films where the sapphire is exposed and excessively nitridized during the initial stages of the 3D GaN growth. The growth method(s) involving a LTNL that protects the sapphire surface from over-nitridation thus leads to GaN epilayers with almost no inversion domains.

5. Conclusion

We have studied the quality of *a*-plane GaN layers grown on *r*-plane sapphire by different MOVPE methods. We find that the presence of a GaN low temperature nucleation layer (LTNL) or its absence (direct growth) does not alter significantly the final material quality in terms of 1D or 2D extended defects: threading dislocations densities (TDDs) are in the low $10^9\,cm^{-2}$ regime and basal plane staking faults densities are greater than $10^5\,cm^{-1}$. The direct growth methods lead to films with high densities of inversion domains (IDs), which may cover up to 40% of the final surface. Without further optimization, the improvements brought by direct growth methods are questionable and better quality layers are produced using SiN_x interlayers. The growth method employing a LTNL combined with a single SiN_x interlayer, '*LT-SiN*', shows the best overall characteristics: a relatively low TDD, almost no IDs, the lowest BSF and PD/PSF signal in the 6K PL spectrum.

With a near isotropic XRD linewidth of ca. 0.14° (500 arcs) for '*LT-SiN*' sample, the crystal quality reported in this work is comparable, if not better, than most of the other hetero-epitaxial *a*-plane GaN layer reported in the literature. Other growth recipes also based on single or multiple SiN_x interlayer [24,15] can yield slightly better results (ca. 400 arcs).

This narrow ω-FWHM could not be correlated with other physical properties such as TD or BSF densities. This conclusion is of significant

importance for the field of *a*-plane GaN layers, in which a significant fraction of the literature mainly relies on XRD to assess the crystal quality of the layers [14–16,18–20,26,23,24,27,29]. The notable exceptions are Song et al. [21], Hao et al. [17], Chakraborty et al. [23], Araki et al. [28] and Johnston et al. [25,22] with some additional AFM and XRD characterizations by Moram et al. [35,32]. Defect densities derived in these detailed studies are comparable to those of obtained here. It is important to note that TEM is currently the only technique that can quantitatively assess BSFs densities. DIC microscopy, AFM, SEM and CL are powerful techniques that together can provide quantitative results on the densities of TDs and IDs along with some optical properties. However they can only provide qualitative results for the density of BSFs, even when combined with dedicated low temperature PL experiments such as in the present work. Therefore, TEM studies are still required to properly quantify the density of BSFs in *a*-plane GaN material and a better understanding is required to make XRD analysis the principal tool for the quality control of non-polar *a*-plane GaN epilayers, as it is for *c*-plane GaN films.

Finally this study has shown that more work is required to find *in situ* growth methods that effectively reduce the density of BSFs and TDs in *a*-plane GaN epilayers to less than $10^5\ cm^{-1}$ and $10^9\ cm^{-2}$ respectively.

Acknowledgments

This work is supported by the Engineering and Physical Sciences Research Council (United Kingdom) under EP/J003603/1 and EP/H0495331. The European Research Council has also provided financial support under the European Community's Seventh Framework Programme (FP7/2007–2013)/ERC grant agreement no. 279361 (MACONS).

The authors thank M.E. Vickers and M.A. Moram for their assistance during the XRD measurements on the InGaN layer.

References

[1] F. Bernardini, V. Fiorentini, D. Vanderbilt, Spontaneous polarization and piezoelectric constants of iii–v nitrides, Phys. Rev. B 56 (1997) R10024–R10027. http://dx.doi.org/10.1103/PhysRevB.56.R10024, URL ⟨http://link.aps.org/doi/10.1103/PhysRevB.56.R10024⟩.

[2] T. Takeuchi, H. Amano, I. Akasaki, Theoretical study of orientation dependence of piezoelectric effects in wurtzite strained GaInN/GaN heterostructures and quantum wells, Japanese J. Appl. Phys. 39 (2000) 413.

[3] A.E. Romanov, T.J. Baker, S. Nakamura, J.S. Speck, E.U. Group, Strain-induced polarization in wurtzite III-nitride semipolar layers, J. Appl. Phys. 100 (2) (2006) 023522, URL ⟨http://dx.doi.org/10.1063/1.2218385⟩.

[4] T. Zhu, F. Oehler, B.P.L. Reid, R.M. Emery, R.A. Taylor, M.J. Kappers, R.A. Oliver, Non-polar (11–20) InGaN quantum dots with short exciton lifetimes grown by metal-organic vapor phase epitaxy, Appl. Phys. Lett. 102 (25) (2013) 251905 http://dx.doi.org/10.1063/1.4812345, URL ⟨http://scitation.aip.org/content/aip/journal/apl/102/25/10.1063/1.4812345⟩.

[5] R.M. Farrell, E.C. Young, F. Wu, S.P. DenBaars, J.S. Speck, Materials and growth issues for high-performance nonpolar and semipolar light-emitting devices, Semicond. Sci. Technol. 27 (2) (2012) 024001, URL ⟨http://stacks.iop.org/0268-1242/27/i=2/a=024001⟩.

[6] S. Schulz, T.J. Badcock, M.A. Moram, P. Dawson, M.J. Kappers, C.J. Humphreys E.P. O'Reilly, Electronic and optical properties of nonpolar a-plane GaN quantum wells, Phys. Rev. B 82 (2010) 125318. http://dx.doi.org/10.1103/PhysRevB.82.125318.

[7] C.H. Chiu, S.Y. Kuo, M.H. Lo, C.C. Ke, T.C. Wang, Y.T. Lee, H.C. Kuo, T.C. Lu, S.C. Wang, Optical properties of a-plane InGaN/GaN multiple quantum wells on r-plane sapphire substrates with different indium compositions, J. Appl. Phys. 105 (6) (2009) 063105 http://dx.doi.org/10.1063/1.3083074, URL ⟨http://scitation.aip.org/content/aip/journal/jap/105/6/10.1063/1.3083074⟩.

[8] N.F. Gardner, J.C. Kim, J.J. Wierer, Y.C. Shen, M.R. Krames, Polarization anisotropy in the electroluminescence of m-plane InGaN–GaN multiple-quantum-well light-emitting diodes, Appl. Phys. Lett. 86 (11) (2005) 111101 http://dx.doi.org/10.1063/1.1875765, URL ⟨http://scitation.aip.org/content/aip/journal/apl/86/11/10.1063/1.1875765⟩.

[9] H.M. Ng, Molecular-beam epitaxy of GaN/$Al_xGa_{1-x}N$ multiple quantum wells on R-plane (10–12) sapphire substrates, Appl. Phys. Lett. 80 (23) (2002) 4369–4371 http://dx.doi.org/10.1063/1.1484543, URL ⟨http://scitation.aip.org/content/aip/journal/apl/80/23/10.1063/1.1484543⟩.

[10] M.D. Craven, S.H. Lim, F. Wu, J.S. Speck, S.P. DenBaars, Structural characterization of nonpolar (11–20) a-plane GaN thin films grown on (1102) r-plane sapphire, Appl. Phys. Lett. 81 (3) (2002) 469–471 http://dx.doi.org/10.1063/1.1493220, URL: ⟨http://scitation.aip.org/content/aip/journal/apl/81/3/10.1063/1.1493220⟩.

[11] M. Rudzinski, R. Kudrawiec, L. Janicki, J. Serafinczuk, R. Kucharski, M. Zajac, J. Misiewicz, R. Doradzinski, R. Dwilinski, W. Strupinski, Growth of GaN epilayers on c-, m-, a-, and (20.1)-plane GaN bulk substrates obtained by ammonothermal method, J. Cryst. Growth 328 (1) (2011) 5–12 http://dx.doi.org/10.1016/j.jcrysgro.2011.06.027, URL ⟨http://www.sciencedirect.com/science/article/pii/S0022024811005379⟩.

[12] P. Vennéguès, Defect reduction methods for III-nitride heteroepitaxial films grown along nonpolar and semipolar orientations, Semicond. Sci. Technol. 27 (2) (2012) 024004, URL ⟨http://stacks.iop.org/0268-1242/27/i=2/a=024004⟩.

[13] P. Gibart, Metal organic vapour phase epitaxy of GaN and lateral overgrowth, Rep. Prog. Phys. 67 (5) (2004) 667–715, URL ⟨http://stacks.iop.org/0034-4885/67/i=5/a=R02⟩.

[14] X. Ni, Y. Fu, Y. Moon, N. Biyikli, H. Morkoç, Optimization of a-plane GaN growth by MOCVD on r-plane sapphire, J. Cryst. Growth 290 (2006) 166–170. http://dx.doi.org/10.1016/j.jcrysgro.2006.01.008, URL ⟨http://www.sciencedirect.com/science/article/pii/S0022024806000406⟩.

[15] S.-M. Hwang, Y.G. Seo, K.H. Baik, I.-S. Cho, J.H. Baek, S. Jung, T.G. Kim, M. Cho, Demonstration of nonpolar a-plane InGaN/GaN light emitting diode on r-plane sapphire substrate, Appl. Phys. Lett. 95 (7) (2009) 071101. http://dx.doi.org/10.1063/1.3206666, URL ⟨http://link.aip.org/link/?APL/95/071101/1⟩.

[16] S.-N. Lee, J. Kim, H. Kim, Crystalline dependence of optical and interfacial properties of InGaN/GaN quantum wells on nonpolar a-plane GaN/r-sapphire, J. Cryst. Growth 326 (1) (2011) 19–22. http://dx.doi.org/10.1016/j.jcrysgro.2011.01.043 ⟨http://www.sciencedirect.com/science/article/pii/S0022024811000820⟩.

[17] R. Hao, M. Kappers, M. Moram, C. Humphreys, Defect reduction processes in heteroepitaxial non-polar a-plane GaN films, J. Cryst. Growth 337 (2011) 81–86. http://dx.doi.org/10.1016/j.jcrysgro.2011.10.004, URL ⟨http://www.sciencedirect.com/science/article/pii/S0022024811008311⟩.

[18] T. Ko, T. Wang, R. Gao, H. Chen, G. Huang, T. Lu, H. Kuo, S. Wang, Study on optimal growth conditions of a-plane GaN grown on r-plane sapphire by metal-organic chemical vapor deposition, J. Cryst. Growth 300 (2007) 308–313. http://dx.doi.org/10.1016/j.jcrysgro.2006.12.046 ⟨http://www.sciencedirect.com/science/article/pii/S0022024807000498⟩.

[19] R. Chandrasekaran, A.S. Ozcan, D. Deniz, K.F. Ludwig, T.D. Moustakas, Growth of non-polar (1120) and semi-polar (1126) AlN and GaN films on the R-plane sapphire, Phys. Status Solidi C 4 (5) (2007) 1689–1693, URL ⟨http://dx.doi.org/10.1002/pssc.200674288⟩.

[20] C. Chiang, K. Chen, Y. Wu, Y. Yeh, W. Lee, J. Chen, K. Lin, Y. Hsiao, W. Huang, E. Chang, Nonpolar a-plane GaN grown on r-plane sapphire using multilayer AlN buffer by metalorganic chemical vapor deposition, Appl. Surf. Sci. 257 (2011) 2415–2418. http://dx.doi.org/10.1016/j.apsusc.2010.10.059, URL ⟨http://www.sciencedirect.com/science/article/pii/S016943321001425X⟩.

[21] H. Song, J.S. Kim, E.K. Kim, S.-H. Lee, J.B. Kim, J. su Son, S.-M. Hwang, Nonpolar growth and characterization of a-plane InGaN/GaN quantum well structures with different indium compositions, Solid-State Electron. 54 (10) (2010) 1221–1226. http://dx.doi.org/10.1016/j.sse.2010.05.015, selected Papers from ISDRS 2009, URL ⟨http://www.sciencedirect.com/science/article/pii/S0038110110001905⟩.

[22] C.F. Johnston, M.J. Kappers, C.J. Humphreys, Microstructural evolution of nonpolar (11-20) GaN grown on (1-102) sapphire using a 3D–2D method, J. Appl. Phys. 105 (2009) 073102. http://dx.doi.org/10.1063/1.3103305, URL ⟨http://scitation.aip.org/content/aip/journal/jap/105/7/10.1063/1.3103305⟩.

[23] A. Chakraborty, K.C. Kim, F. Wu, J.S. Speck, S.P. DenBaars, U.K. Mishra, Defect reduction in nonpolar a-plane GaN films using in situSiNx nanomask, Appl. Phys. Lett. 89 (2006) 041903. http://dx.doi.org/10.1063/1.2234841 ⟨http://scitation.aip.org/content/aip/journal/apl/89/4/10.1063/1.2234841⟩.

[24] J.L. Hollander, M.J. Kappers, C. McAleese, C.J. Humphreys, Improvements in a-plane GaN crystal quality by a two-step growth process, Appl. Phys. Lett. 92 (10) (2008) 101104. http://dx.doi.org/10.1063/1.2830023.

[25] C. Johnston, M. Kappers, M. Moram, J. Hollander, C. Humphreys, Assessment of defect reduction methods for nonpolar a-plane GaN grown on r-plane sapphire, J. Cryst. Growth 311 (2009) 3295–3299. http://dx.doi.org/10.1016/j.jcrysgro.2009.03.044, URL ⟨http://www.sciencedirect.com/science/article/pii/S0022024809004047⟩.

[26] M. Wieneke, M. Noltemeyer, B. Bastek, A. Rohrbeck, H. Witte, P. Veit, J. Blasing, A. Dadgar, J. Christen, A. Krost, Heavy Si doping: the key in heteroepitaxial growth of a-plane GaN without basal plane stacking faults? Phys. Status Solidi B 248 (3) (2011) 578–582, URL ⟨http://onlinelibrary.wiley.com/doi/10.1002/pssb.201046372/full⟩.

[27] M. Araki, K. Hoshino, K. Tadatomo, Direct growth of a-plane GaN on r-plane sapphire substrate by metalorganic vapor phase epitaxy, Phys. Status Solidi C 4 (2007) 2540–2543. http://dx.doi.org/10.1002/pssc.200674829, URL ⟨http://onlinelibrary.wiley.com/doi/10.1002/pssc.200674829/abstract⟩.

[28] M. Araki, N. Mochimizo, K. Hoshino, K. Tadatomo, Effect of misorientation angle of r-plane sapphire substrate on a-plane GaN grown by metalorganic vapor phase epitaxy, Jpn. J. Appl. Phys. 47 (2008) 119–123. http://dx.doi.org/10.7567/JJAP.47.119, URL ⟨http://jjap.jsap.jp/link?JJAP/47/119/⟩.

[29] R. Miyagawa, M. Narukawa, B. Ma, H. Miyake, K. Hiramatsu, Reactor-pressure dependence of growth of a-plane GaN on r-plane sapphire by MOVPE, J. Cryst. Growth 310 (2008) 4979–4982. http://dx.doi.org/10.1016/j.jcrysgro.2008.08.027, URL ⟨http://www.sciencedirect.com/science/article/pii/S0022024808007227⟩.

[30] C. Roder, S. Einfeldt, S. Figge, T. Paskova, D. Hommel, P.P. Paskov, B. Monemar, U. Behn, B.A. Haskell, P.T. Fini, S. Nakamura, Stress and wafer bending of a-plane GaN layers on r-plane sapphire substrates, J. Appl. Phys. 100 (10) (2006) 103511. http://dx.doi.org/10.1063/1.2386940, URL ⟨http://link.aip.org/link/?JAP/100/103511/1⟩.
[31] R. Oliver, M. Kappers, J. Sumner, R. Datta, C. Humphreys, Highlighting threading dislocations in MOVPE-grown GaN using an in situ treatment with SiH_4 and NH_3, J. Cyst. Growth 289 (2) (2006) 506–514, URL ⟨http://linkinghub.elsevier.com/retrieve/pii/S0022024805015769⟩.
[32] M.A. Moram, C.F. Johnston, M.J. Kappers, C.J. Humphreys, Measuring dislocation densities in nonpolar a -plane GaN films using atomic force microscopy, J. Phys. D: Appl. Phys. 43 (5) (2010) 055303, URL ⟨http://stacks.iop.org/0022-3727/43/i=5/a=055303⟩.
[33] I. Kim, H. Park, Y. Park, T. Kim, Formation of V-shaped pits in InGaN/GaN multiquantum wells and bulk InGaN films, Appl. Phys. Lett. 73 (1998) 1634, URL ⟨http://link.aip.org/link/?APPLAB/73/1634/1⟩.
[34] Q. Sun, B.H. Kong, C.D. Yerino, T.-S. Ko, B. Leung, H.K. Cho, J. Han, Morphological and microstructural evolution in the two-step growth of nonpolar a-plane GaN on r-plane sapphire, J. Appl. Phys. 106 (12) (2009) 123519, journal article, URL ⟨http://dx.doi.org/10.1063/1.3272790⟩.
[35] M.A. Moram, M.E. Vickers, X-ray diffraction of III-nitrides, Rep. Prog. Phys. 72 (2009) 036502. http://dx.doi.org/10.1088/0034-4885/72/3/036502.
[36] M.E. Vickers, J.L. Hollander, C. McAleese, M.J. Kappers, M.A. Moram, C.J. Humphreys, Determination of the composition and thickness of semi-polar and non-polar III-nitride films and quantum wells using X-ray scattering, J. Appl. Phys. 111 (4) (2012) 043502. http://dx.doi.org/10.1063/1.3678631, URL ⟨http://link.aip.org/link/?JAP/111/043502/1⟩.
[37] F. Oehler, M.E. Vickers, M.J. Kappers, C.J. Humphreys, R.A. Oliver, Fundamentals of X-ray diffraction characterisation of strain in GaN based compounds, Jpn. J. Appl. Phys. 52 (2013) 08JB29. http://dx.doi.org/10.1143/JJAP.52.08JB29, URL ⟨http://jjap.jsap.jp/link?JJAP/52/08JB29/⟩.
[38] P.F. Fewster, X-ray Scattering from Semiconductors, 2nd edition, Imperial College Press, 2003.
[39] A. Krost, A. Dadgar, G. Strassburger, R. Clos, GaN-based epitaxy on silicon: stress measurements, Phys. Status Solidi A 200 (1) (2003) 26–35. http://dx.doi.org/10.1002/pssa.200303428.
[40] C. Roder, S. Einfeldt, S. ablege, D. Hommel, Temperature dependence of the thermal expansion of GaN, Phys. Rev. B 72 (2005) 085218. http://dx.doi.org/10.1103/PhysRevB.72.085218.
[41] P. Corfdir, P. Lefebvre, J. Ristić, J.-D. Ganière, B. Deveaud-Plédran, Electron localization by a donor in the vicinity of a basal stacking fault in GaN, Phys. Rev. B 80 (2009) 153309. http://dx.doi.org/10.1103/PhysRevB.80.153309.
[42] P. Corfdir, P. Lefebvre, J. Levrat, A. Dussaigne, J.-D. Ganière, D. Martin, J. Ristic, T. Zhu, N. Grandjean, B. Deveaud-Plédran, Exciton localization on basal stacking faults in a-plane epitaxial lateral overgrown GaN grown by hydride vapor phase epitaxy, J. Appl. Phys. 105 (4) (2009) 043102 http://dx.doi.org/10.1063/1.3075596, URL ⟨http://scitation.aip.org/content/aip/journal/jap/105/4/10.1063/1.3075596⟩.
[43] B. Monemar, P.P. Paskov, J.P. Bergman, A.A. Toropov, T.V. Shubina, T. Malinauskas, A. Usui, Recombination of free and bound excitons in GaN, Phys. Status Solidi B 245 (9) (2008) 1723–1740, URL ⟨http://dx.doi.org/10.1002/pssb.200844059⟩.
[44] D.N. Zakharov, Z. Liliental-Weber, B. Wagner, Z.J. Reitmeier, E.A. Preble, R. F. Davis, Structural TEM study of nonpolar a-plane GaN grown on (11-20) 4 H-SiC by organometallic vapor phase epitaxy, Phys. Rev. B 71 (23) (2005) 235334, URL ⟨http://link.aps.org/doi/10.1103/PhysRevB.71.235334⟩.
[45] P. Vennéguès, Z. Bougrioua, T. Guehne, Microstructural characterization of semi-polar GaN templates and epitaxial-lateral-overgrown films deposited on m-plane sapphire by metalorganic vapor phase epitaxy, Jpn. J. Appl. Phys. 46 (2007) 4089.
[46] M. Haberlen, T.J. Badcock, M.A. Moram, J.L. Hollander, M.J. Kappers, P. Dawson, C.J. Humphreys, R.A. Oliver, Low temperature photoluminescence and cathodoluminescence studies of nonpolar GaN grown using epitaxial lateral overgrowth, J. Appl. Phys. 108 (3) (2010) 033523. http://dx.doi.org/10.1063/1.3460641 ⟨http://link.aip.org/link/?JAP/108/033523/1⟩.
[47] M.B. McLaurin, A. Hirai, E. Young, F. Wu, J.S. Speck, Basal plane stacking-fault related anisotropy in X-ray rocking curve widths of *m*-plane GaN, Jpn. J. Appl. Phys. 47 (7) (2008) 5429–5431. http://dx.doi.org/10.1143/JJAP.47.5429, URL ⟨http://jjap.jsap.jp/link?JJAP/47/5429/⟩.
[48] M.A. Moram, C.F. Johnston, J.L. Hollander, M.J. Kappers, C.J. Humphreys, Understanding x-ray diffraction of nonpolar gallium nitride films, J. Appl. Phys. 105 (11) (2009) 113501. http://dx.doi.org/10.1063/1.3129307, URL ⟨http://link.aip.org/link/?JAP/105/113501/1⟩.
[49] Q. Sun, C.D. Yerino, B. Leung, J. Han, M.E. Coltrin, Understanding and controlling heteroepitaxy with the kinetic Wulff plot: a case study with GaN, J. Appl. Phys. 110 (5) (2011) 053517, URL ⟨http://dx.doi.org/10.1063/1.3632073⟩.
[50] G. Li, S.J. Chua, S.J. Xu, W. Wang, P. Li, B. Beaumont, P. Gibart, Nature and elimination of yellow-band luminescence and donor-acceptor emission of undoped GaN, Appl. Phys. Lett. 74 (19) (1999) 2821–2823 http://dx.doi.org/10.1063/1.124025, URL ⟨http://scitation.aip.org/content/aip/journal/apl/74/19/10.1063/1.124025⟩.
[51] S.F. Chichibu, A. Setoguchi, A. Uedono, K. Yoshimura, M. Sumiya, Impact of growth polar direction on the optical properties of GaN grown by metalorganic vapor phase epitaxy, Appl. Phys. Lett. 78 (1) (2001) 28–30 http://dx.doi.org/10.1063/1.1337641, URL ⟨http://scitation.aip.org/content/aip/journal/apl/78/1/10.1063/1.1337641⟩.
[52] J. Rouvière, M. Arlery, R. Niebuhr, K. Bachem, O. Briot, Transmission electron microscopy characterization of GaN layers grown by MOCVD on sapphire, Mater. Sci. Eng. B 43 (1–3) (1997) 161–166, URL ⟨http://www.sciencedirect.com/science/article/pii/S0921510796018557⟩.
[53] M. Sumiya, K. Yoshimura, T. Ito, K. Ohtsuka, S. Fuke, K. Mizuno, M. Yoshimoto, H. Koinuma, A. Ohtomo, M. Kawasaki, Growth mode and surface morphology of a GaN film deposited along the N-face polar direction on c-plane sapphire substrate, J. Appl. Phys. 88 (2) (2000) 1158–1165 http://dx.doi.org/10.1063/1.373791, URL ⟨http://scitation.aip.org/content/aip/journal/jap/88/2/10.1063/1.373791⟩.